Structure, microstructure and thermoelectric properties of germanite-type Cu22Fe8Ge4S32 compounds

L. Paradis-Fortin, G. Guélou, V. Pavan Kumar, P. Lemoine, C. Prestipino, O. Merdrignac-Conanec, G.R. Durand, Stéphane Cordier, O.I. Lebedev, E. Guilmeau

To cite this version:

L. Paradis-Fortin, G. Guélou, V. Pavan Kumar, P. Lemoine, C. Prestipino, et al.. Structure, microstructure and thermoelectric properties of germanite-type Cu22Fe8Ge4S32 compounds. Journal of Alloys and Compounds, 2020, 831, pp.154767. ⟨10.1016/j.jallcom.2020.154767⟩. ⟨hal-02569943⟩

IMPORTANT

The final version has undergone significant change prior to publication, especially 2 references from this PDF file have been removed.

Sample CRediT author statement

L. Paradis-Fortin: Methodology, Investigation, Writing - Original Draft. **G. Guélou**: Investigation, Writing - Review & Editing. **V. Pavan Kumar**: Conceptualization, Investigation. **P. Lemoine**: Conceptualization, Methodology, Investigation, Writing - Review & Editing. **C. Prestipino**: Investigation. **O. Merdrignac-Conanec**: Investigation, Writing - Review & Editing. **G. R. Durand**: Investigation, Writing - Review & Editing. **S. Cordier**: Supervision. **O. I. Lebedev**: Investigation. **E. Guilmeau**: Conceptualization, Supervision, Methodology, Investigation, Writing - Review & Editing.

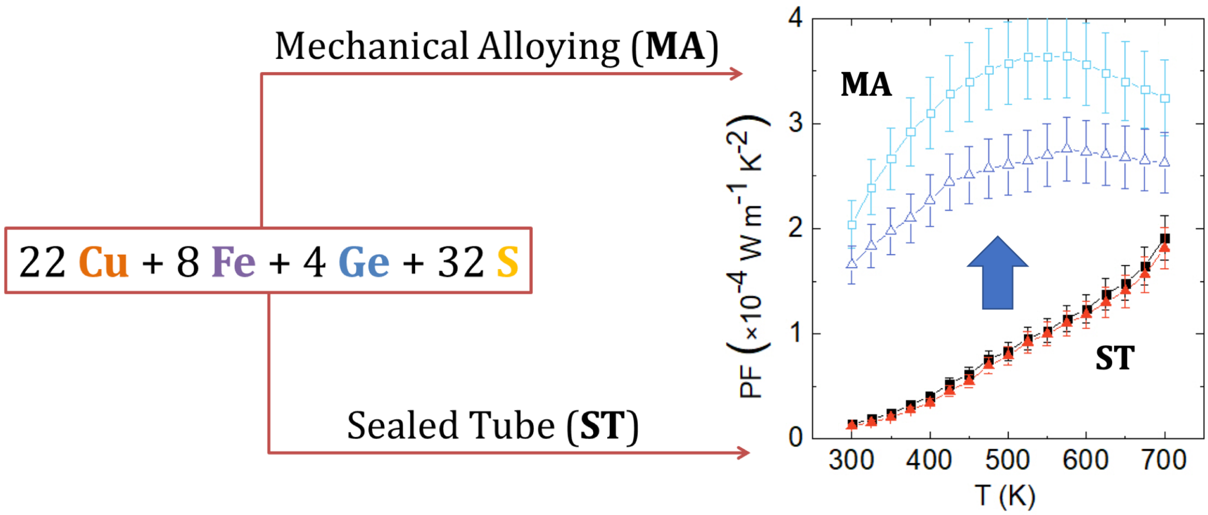
Mechanical Alloying (**MA**)
22 Cu + 8 Fe + 4 Ge + 32 S
Sealed Tube (**ST**)
MA
ST
PF $(\times 10^{-4}\ \mathrm{W\ m^{-1}\ K^{-2}})$
0
1
2
3
4
300
400
500
600
700
T (K)

Structure, microstructure and thermoelectric properties of germanite-type $Cu_{22}Fe_8Ge_4S_{32}$ compounds

L. Paradis-Fortin[a,b], G. Guélou[a], V. Pavan Kumar[a], P. Lemoine[b,*], C. Prestipino,[b] O. Merdrignac-Conanec[b], G. R. Durand[b], S. Cordier[b], O. I. Lebedev[a] and E. Guilmeau[a,*]

[a] CRISMAT, CNRS, Normandie Univ, ENSICAEN, UNICAEN, 14000 Caen, France

[b] Univ Rennes, CNRS, ISCR – UMR 6226, F-35000 Rennes, France

Corresponding authors : emmanuel.guilmeau@ensicaen.fr; pierric.lemoine@univ-rennes1.fr

Abstract

This paper describes the influence of the powder synthesis and densification techniques on the structure, microstructure and thermoelectric properties of $Cu_{22}Fe_8Ge_4S_{32}$, a synthetic derivative of the naturally occurring germanite mineral. Two powder synthesis approaches are compared, namely mechanical alloying and conventional sealed tube synthesis, combined with two densification methods: spark plasma sintering and hot pressing. Structural analyses by Le Bail refinement of X-ray powder diffraction patterns and transmission electron microscopy confirmed the high crystallinity and the absence of structural defects in the samples. It is especially highlighted that mechanical alloying combined with low sintering temperature allows to reach high purity and to limit the formation of secondary phases due to sulfur volatilization in the bulk specimens. The changes in the electrical resistivity and Seebeck coefficient with the sample preparation methods evidence the high sensitivity of the material to slight stoichiometric

deviations. Conversely, the thermal conductivity is less influenced by stoichiometric variations and microstructural changes. This investigation draws attention to the significant impact of powder synthesis and sintering methods on the electrical transport properties of complex quaternary Cu-based sulfides specifically designed to present intrinsically low thermal conductivity for potential thermoelectric applications.

Introduction

To address the socio-environmental issues engendered by the ever-growing energy demand, drastic changes in energy management must be anticipated. This context favored a renewal in the interest on thermoelectric (TE) technology.[1] TE performances are quantified by the dimensionless figure of merit $ZT = S^2T/\rho\kappa$, where T is the absolute temperature (K), S is the Seebeck coefficient (V K^{-1}), ρ is the electrical resistivity (Ω m), and κ is the total thermal conductivity (W m^{-1} K^{-1}).[2] Beyond the promising results obtained for telluride-based materials which exhibit high performances,[3–5] the need to conciliate efficiency with environmental and cost constraints has triggered research toward copper-based sulfides, which, for most of them, benefit from containing eco-friendly and abundant elements. Tetrahedrite $Cu_{12}Sb_4S_{13}$,[6–15] colusite $Cu_{26}V_2Sn_6S_{32}$,[16–23] stannoidite $Cu_8Fe_3Sn_2S_{12}$,[24–26] and bornite Cu_5FeS_4[27–30] are a few of the naturally occurring Cu-based sulfide minerals that have been reported to date for their promising thermoelectric properties.

Due to the high sensitivity of sulfur to volatilize during the processing route, the synthesis techniques are of prime importance and can critically alter the final chemical composition and modify the structure, the microstructure and the electrical and thermal properties. A stoichiometric deviation can cause a drastic change in charge carrier concentration to an extent where the whole electrical and thermal transport behaviors are different. For instance, a drastic change of behavior was reported for the *n*-type $Cu_4Sn_7S_{16}$.[31] In fact, while the samples synthesized by mechanical alloying (MA) show a semiconducting behavior, as reported in previous works,[32,33] the sample synthesized by conventional sealed tube (ST) synthesis exhibits a metallic behavior due to minor stoichiometry deviations. Another crucial step in the handling of sulfide materials resides in the sintering process. Often overlooked, it can also modify the structural and microstructural features of the material, and induce significant changes in the electrical and thermal properties. One of the highest *ZT* value (*i.e.* 0.93 at 675 K) among sulfide materials [16,23] was recently achieved in colusite $Cu_{26}V_2Sn_6S_{32}$ by lowering its thermal conductivity while maintaining its power factor ($PF = S^2/\rho$) through the control of the sintering conditions. The lattice thermal conductivity was decreased from 1.35 W m^{-1} K^{-1} to 0.35 W m^{-1} K^{-1} at 300 K by increasing the sintering temperature from 873 K (Spark Plasma Sintering, SPS) to 1023 K (Hot Pressing, HP). This drastic κ reduction was largely attributed to the enhanced phonon scattering induced by the formation of point defects and disordered regions in the sample sintered at higher temperature.

Recently, we reported on the synthesis of $Cu_{22}Fe_8Ge_4S_{32}$, a derivative of the naturally occurring germanite mineral, $Cu_{26}Fe_4Ge_4S_{32}$.[34] This phase kept our attention because of its close structural relationships to colusite, hence giving the possibility that they share a common intrinsically low lattice thermal conductivity and high power factor. Unfortunately, the power factor of this material is found relatively low (0.34 mW m^{-1} K^{-2} at 575 K) and the lattice thermal conductivity (κ_L) of germanite, *c.a.* 1.76 W m^{-1} K^{-1} at 300 K, is comparable to that of the ordered $Cu_{26}V_2Sn_6S_{32}$ colusite. This leads to a maximum *ZT* value of 0.14 at 575 K, comparable to that of colusite $Cu_{26}V_2Sn_6S_{32}$ sintered in similar conditions (*i.e.* at 873 K for 30 min under a pressure of 64 MPa).[16,21] Considering that the synthesis methods can strongly affect the electrical and thermal properties of such compounds due to their high sensitivity to sulfur loss and their ability to promote structural disordering, we have investigated the effect of powder synthesis and densification techniques on the structure, microstructure and thermoelectric properties of a synthetic germanite-derivative $Cu_{22}Fe_8Ge_4S_{32}$.

Experimental

In this study, by combining two different powder syntheses (MA or ST) and two sintering processes (SPS or HP), four samples of germanite $Cu_{22}Fe_8Ge_4S_{32}$ were synthesized, namely MA_SPS, MA_HP, ST_SPS and ST_HP.

For both synthesis methods, Cu (99 %, Alfa Aesar), Fe (99.5 %, Alfa Aesar), S (99.5 %, Alfa Aesar), and Ge (99.999 %, Alfa Aesar) commercial powders, were stored and manipulated in a glove box under argon atmosphere. The starting materials for both mechanically alloyed and sealed tube samples were weighted in a stoichiometric ratio and ground in an agate mortar. For the synthesis of the mechanically alloyed samples, two batches of 4 g each were prepared and put into two 45 mL tungsten carbide jars along with a total of 14 balls with a diameter of $\Phi = 10$ mm, for a 13:1 ball-to-powder weight ratio. The milling lasted for 360 min at 600 rpm decomposed in 24 cycles of 15 min each with 1 min pause and a reverse of the milling direction. For the synthesis of the sealed tube samples, 4 g batches of powder were pressed into eight pellets of ~ 0.5 g with a $\Phi = 5$ mm die. This procedure was intended to favor solid state diffusion and enhance the effective surface for the solid-liquid-gas interactions. The pellets were placed in sealed silica tubes evacuated down to a pressure of ~ 10^{-2} mbar from an argon atmosphere. The reaction was performed in a vertical tubular furnace with a heating rate of 2 K min^{-1} and a plateau at 973 K for 24 h. The sample was cooled down to 773 K at a natural cooling rate and then air quenched.

Powders (*ca*. 3 g) from the ST or MA synthesis were weighted and put into a graphite die (Φ = 10 mm) and densified by SPS at 873 K under a uniaxial pressure of 64 MPa with a heating rate of 30 K min^{-1} and a holding time of 30 min in a spark plasma sintering furnace (SPS-FCT HPD 25) under static secondary vacuum. The hot-pressed samples (*ca*. 3 g) were sintered in a graphite die (Φ = 10 mm), at 873 K under a uniaxial pressure of 64 MPa with a heating rate of 15 K min^{-1} and a holding time of 60 min under dynamic primary vacuum (about 0.3 mbar) in a VAS (*Vide et Appareils Scientifiques*) equipment. The sintering temperature of 873 K was fixed according to a previous study,[34] where high purity samples were obtained.

The samples were characterized before and after sintering by X-ray powder diffraction (XRPD), using a two-circle diffractometer (D8 Advance Vario1) equipped with a copper anticathode X-ray tube ($K\alpha_1$ = 1.5406 Å) and a silicon band LynxEye detector ($K\alpha_2$ and Kβ radiations are filtered out by a Ge [111] monochromator). Data were collected over the angular range 5 – 80° with a step size of 0.019699° and a step time of 7 s. Le Bail refinements were carried out using Fullprof and WinPlotr softwares packages.[35,36] Peak shape profile was refined with a Thompson-Cox-Hastings pseudo-Voigt convoluted with axial divergence asymmetry function.[37]

Scanning electron microscopy (SEM) observations of a fractured cross-section and of mirror-polished surfaces of the densified pellets were performed using ZEISS Supra 55 and JEOL Multifonctions 7200 LV microscopes, equipped with Quantax Brukker electron dispersive spectrometer. Transmission electron microscopy (TEM) analysis including electron diffraction (ED) and high angle annular dark field scanning TEM (HAADF-STEM) studies were performed by using a JEM200F cold FEG image and probe aberration microscope operated at 200 kV, equipped with CENTURIO EDX detector and Quantum GIF. The samples were deposited on a Ni holey carbon grid in an *n*-butanol suspension.

Electrical resistivity and Seebeck coefficient were measured on an Ulvac Riko ZEM3 measuring system under partial pressure of helium to ease the stabilization of the temperature gradient. The properties were measured on bars (*ca*. 2.5 × 2.5 × 8 mm^3) from RT to 673 K. A Netzsch LFA 457 system was used to measure the thermal diffusivity under dynamic nitrogen flow. The measurements were done in an airtight furnace under a nitrogen atmosphere between 300 K and 673 K with 50 K increments on 6 × 6 mm^2 and 1 mm thick samples. Thermal conductivity, κ, was determined from the product of thermal diffusivity, density and the specific heat capacity obtained from the Dulong-Petit approximation (0.42 J g^{-1} K^{-1}). The electronic contribution of the thermal conductivity, κ_{el}, was estimated from the Wiedemann–Franz law with the Lorenz number approximated from the Seebeck coefficient using the simplified relationship, $L = 1.5 + \exp(-|S|/116)$ from Kim *et al*.[38] The lattice thermal conductivity, κ_L ,was obtained by subtracting the electronic contribution from the total thermal conductivity. Hall effect measurements were carried out from 300 K to 5 K using a Physical Properties Measurement System (PPMS Quantum Design) in an applied magnetic field up to 7 T. However, we were not able to extract reliable carrier concentrations due to an anomalous contribution. Attempts to calculate the carrier concentration using the approximation of single parabolic band conduction model gave unrealistic values. The estimated measurement uncertainties are 6 % for the Seebeck coefficient, 8 % for the electrical resistivity, 11 % for the thermal conductivity, and 16 % for the final figure of merit, *ZT*.[39]

Results

Synthetic germanite $Cu_{22}Fe_8Ge_4S_{32}$ ($P\bar{4}3n$, a = 10.59 Å, V = 1188 Å^3) is a compound with a superstructure (2 a × 2 a × 2 a) derived from the cubic sphalerite ZnS ($F\bar{4}3m$, a = 5.41 Å, V = 158 Å^3), with cations distributed on five different crystallographic sites: 2*a*, 6*c*, 6*d*, 8*e*, and 12*f*, all tetrahedrally coordinated by four sulfur atoms distributed on two different crystallographic sites (8*e* and 24*i*). In a recent study, Pavan Kumar *et al.*[34] proposed approximate structural models for synthetic germanite $Cu_{22}Fe_8Ge_4S_{32}$, established on the basis of a cationic distribution close to that reported for natural germanite $Cu_{26}Fe_4Ge_4S_{32}$.[40] The difficulties to determine the cationic arrangement of synthetic germanite stem from the similarity between cationic sites (same coordination and comparable site sizes), the presence of mixed occupancies and the nature of the cations (equivalent electronic density). Currently, a structural model that successfully accounts for all the observed superstructure reflections has yet to be confirmed. An in-depth structural analysis is on-going using large-scale facilities data (synchrotron/neutron diffraction) and is outside the scope of this study. Consequently, XRPD data refinements in this study were performed using the Le Bail method.

The XRPD patterns of the two batches of powders before sintering process are presented in **Figure 1** and the XRPD patterns of the four samples (after SPS or HP) are presented in **Figure 2**. As shown in **Figure 1a**, the XRPD pattern of the pre-reacted mechanically alloyed powder shows broad diffraction peaks belonging to the main reflections of the sphalerite lattice (sub-structure of germanite). Small diffraction peaks are attributed to unreacted elementary Ge. SEM images of mechanochemically synthesized powders are given in **Figure 3a and 3b.** Polydisperse distribution of particles can be observed with the tendency to form aggregated grains of few hundred of nanometers. The reactive sintering by SPS at 873 K of the MA powder (MA_SPS) yields a high purity sample with a lattice parameter a = 10.5884(1) Å (**Figure 2a**). While the main diffraction peaks are attributed to the sphalerite lattice, the additional superstructure reflections at low angles resulting from the doubling of the unit cell parameter in the three directions confirm the crystallization of a germanite-type phase. Similarly, the reactive sintering of the MA powders by HP (MA_HP) leads to a high purity germanite-type phase with a cell parameter a = 10.5908(2) Å and traces of a nukundamite phase. (**Figure 2b**).

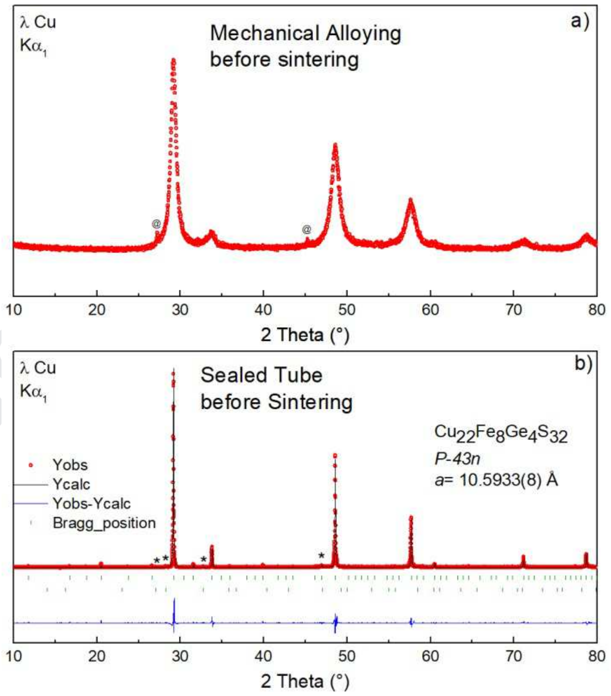

Figure 1. Le Bail refinements of the XRPD patterns of (a) mechanically alloyed and (b) sealed tube powders. The MA sample displays two well crystallized peaks (identified by a @ sign) belonging to unreacted Ge. The ST sample contains a small portion of bornite Cu_5FeS_4, which main peaks are identified by an asterisk (*). Red dots, black and blue curves represent the observed, calculated and difference patterns respectively. The green vertical lines represent the central position of the Bragg reflections of germanite (top) and bornite (bottom).

The powder sample obtained from sealed tube (ST) synthesis is found to be well crystallized with only traces of bornite (Cu_5FeS_4) in its cubic HT form as seen on **Figure 1b**. The superstructure reflections at low angles confirm the formation of the germanite-type phase. SEM images (**Figure 3c and 3d**) show that the powders are composed of large agglomerates. The grain size is significantly larger as compared to powders prepared by mechanical alloying, as the long synthesis duration at high temperature in sealed tube (973 K/24 h) favors the elements diffusion and the growth of large crystallites/grains. Sintering the ST powders by SPS (ST_SPS) or HP (ST_HP) at 873 K leads to a slight increase of the cell parameter from a = 10.5933(8) Å for the as-synthesized powder to a = 10.5969(1) Å and 10.5986(1) Å for the ST_SPS and ST_HP samples, respectively. Note that for ST powders, sintering tends to slightly increase the intensity of the diffraction peaks related to the bornite phase **(Figure 2c** and **2d**). On the other hand, cell parameter disparities can be observed between the four samples. While this difference is negligible for the powders synthesized by the same method, it is more pronounced between the samples synthesized from MA or ST powders such as: ST_HP (10.5986 Å) & ST_SPS (10.5969 Å) > MA_HP (10.5908 Å) & MA_SPS (10.5884 Å). The larger cell parameter in ST-based samples likely originates from sulfur loss due to longer exposure to high temperature. Indeed, as in colusite $Cu_{26}V_2Sn_6S_{32}$ and $Cu_{26}Nb_2Sn_6S_{32}$,[16,23,41,42] the sulfur loss favors structural disorder including interstitial sites and anti-sites defects, leading to an increase of the cell parameter.

SEM analyses performed on mirror-polish surfaces of MA_SPS confirm a homogeneous composition close to the nominal one (within the error of measurements, **Fig. 4a** and **4b**), with only minor traces of WC (**Fig. 4a**) and bornite (**Fig. 4b**), not detectable in the XRD patterns. On the contrary, the ST_SPS sample (**Figure 4c** and **4d**) presents large inclusions of bornite phase, as observed in the XRD pattern. Nevertheless, the composition of the matrix does not show significant difference with the one measured in the MA_SPS sample.

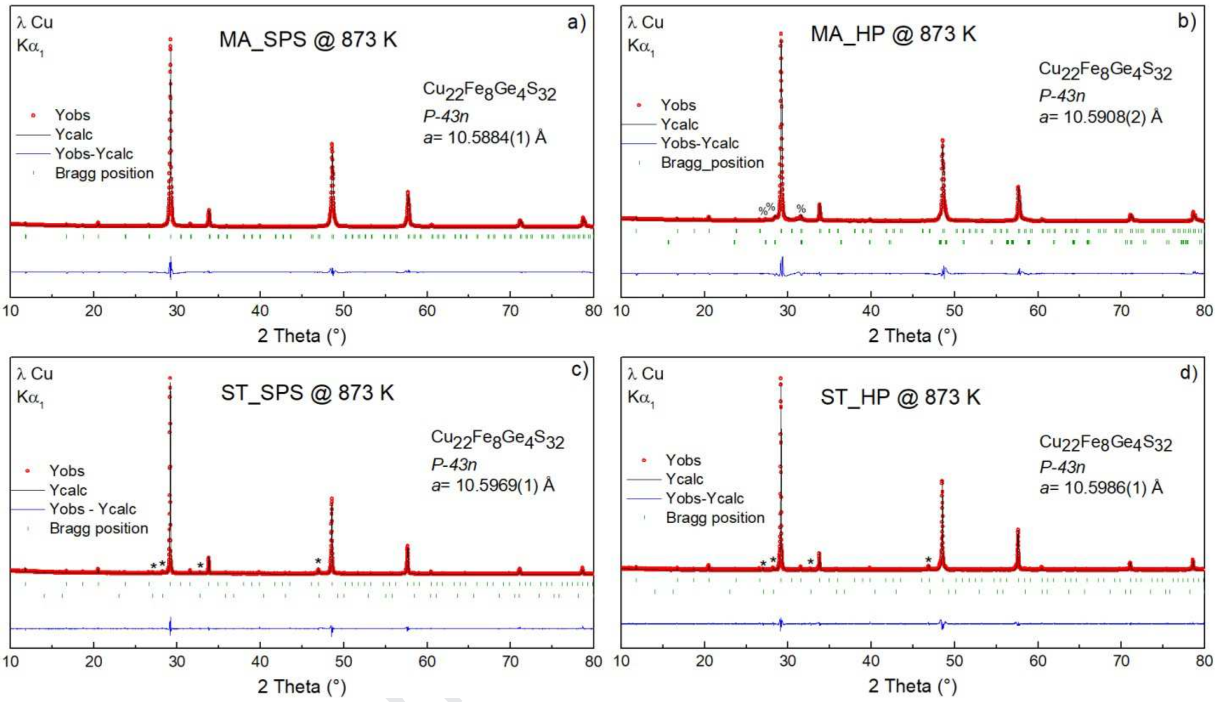

Figure 2. Le Bail refinements of the XRPD patterns of a) MA_SPS, b) MA_HP, c) ST_SPS and d) ST_HP samples. Both ST samples contain a small portion of bornite, whose main peaks are identified by an asterisk (*) and MA_HP contains a small fraction of nukundamite, identified by a percent (%) sign. Red dots, black and blue curves represent the observed, calculated and difference patterns respectively. The green vertical lines represent the central position of the Bragg reflections of germanite (top) and secondary phase (bottom).

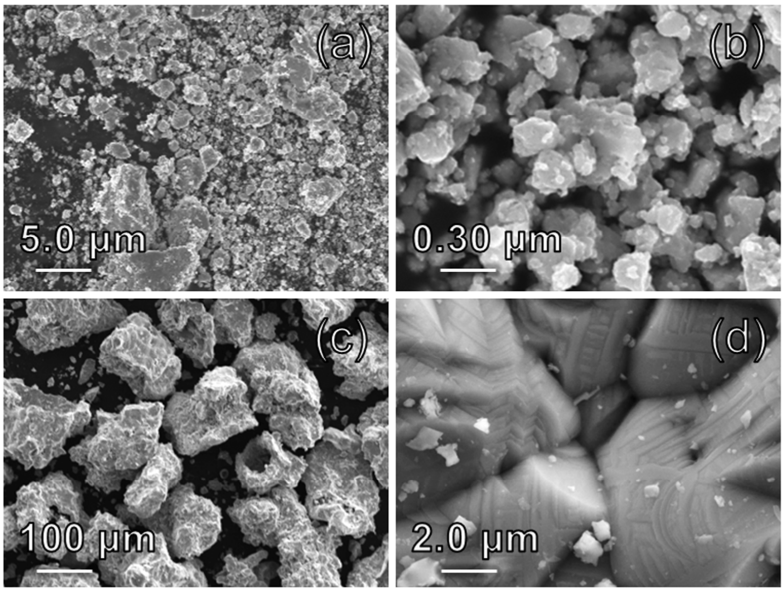

Figure 3. Micrographs of powders synthesized by mechanical alloying (a,b) or sealed tube synthesis (c,d).

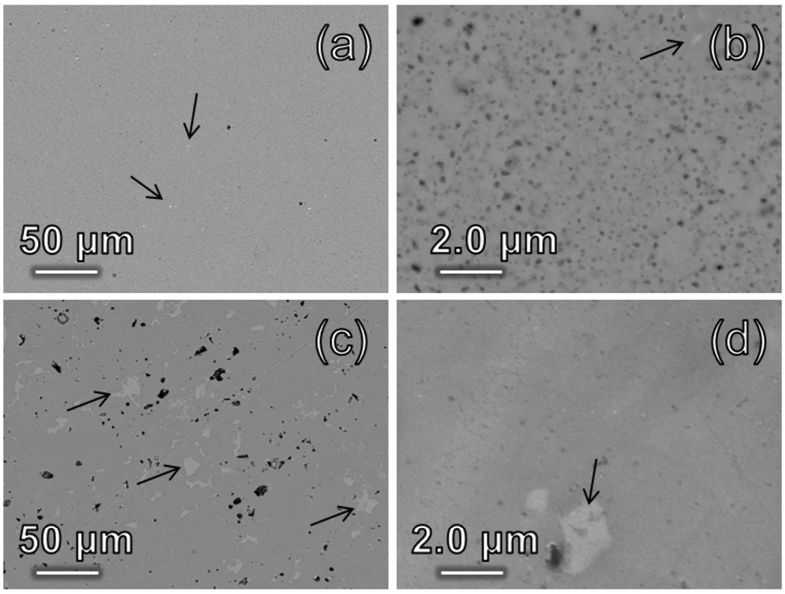

Figure 4. Micrographs of mirror-polish surfaces for a) and b) MA_SPS and for c) and d) ST_SPS samples. Arrows in a) indicate WC particles (white). Arrows in b), c) and d) indicate bornite phase (light grey).

SEM micrographs of the fractured cross-sections of the sintered samples are displayed in **Figure 5**. The micrographs evidence a fine and homogeneous microstructure for both MA_SPS and MA_HP samples (**Figure 5a** and **5b**, respectively). Relative geometrical densities of MA_SPS and MA_HP samples of about 95.0 % and 96.2 %, respectively, are consistent with the residual porosity observed in the SEM images. The estimated average particle size, determined by the intercept method, for the MA_HP sample is around 0.60 ± 0.10 µm, which is slightly larger than that of the MA_SPS sample (0.40 ± 0.10) µm, in agreement with the longer dwell time (and lower heating rate) used during hot pressing. The grain sizes of ST_SPS and ST_HP samples were found to be significantly larger **(Figure 5c** and **5d**, respectively), with an average value around 7.0 ± 0.5 µm, in accordance with the larger crystallites size of the initial powders (**Figure 3**). As expected, sealed tube and mechanical alloying syntheses yield a mean grain size difference of an order of magnitude. The long synthesis duration at high temperature (973 K/24 h) favors the elements diffusion and the growth of large crystallites/grains compared to the repeated welding, fracturing, and rewelding mechanisms involved during mechanical alloying that leads to small particle sizes.[43] Moreover, ST_SPS and ST_HP samples present relative densities of 96.7 % and 99.4 %, respectively, which are slightly higher than those of MA_SPS and MA_HP samples.

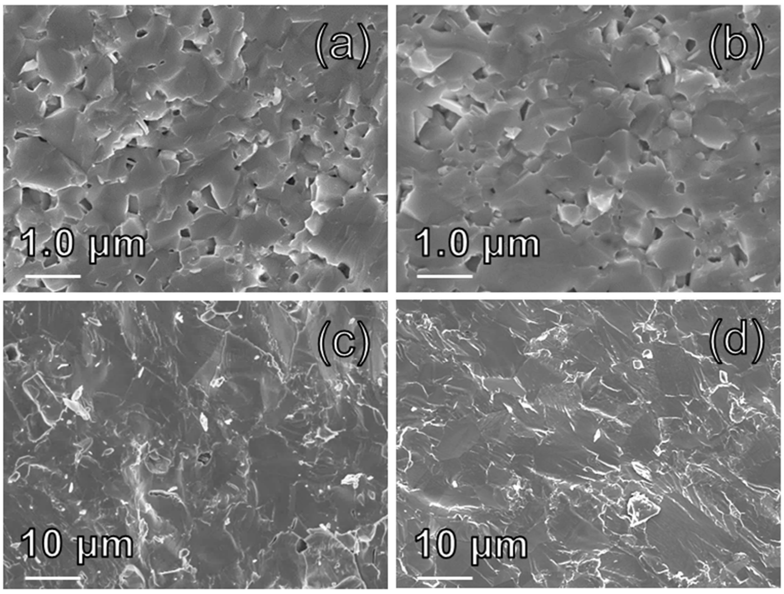

Figure 5. Micrographs of fractured cross-sections for a) MA_SPS b) MA_HP c) ST_SPS and d) ST_HP sintered samples.

Thermoelectric properties

The temperature dependence of the Seebeck coefficient (*S*), given in **Figure 6a**, shows that all the compounds are *p*-type with *S* values ranging from 93 μV K^{-1} to 329 μV K^{-1} at 300 K. The Seebeck coefficient of MA_SPS and MA_HP samples increases with temperature from 300 K to 450 K, but suddenly manifests a change in its temperature dependence. This behavior can be explained by the fact that the electrical conduction is in an intermediate regime between metallic and semiconducting behavior.[34] The Seebeck coefficient of ST_SPS and ST_HP is decreasing over the full temperature range exhibiting a semiconducting behavior. Both ST samples display higher Seebeck coefficient than their MA counterparts, with values of 329 μV K^{-1} for ST_SPS, 279 μV K^{-1} for ST_HP, 133 μV K^{-1} for MA_SPS and 93 μV K^{-1} for MA_HP at RT. As the Seebeck coefficient is directly proportional to the charge carrier effective mass (m^*), a property considered to be invariant in this series of samples, and inversely proportional to the charge carrier concentration, it is likely that the changes in the amplitude of the Seebeck coefficient between the four samples is caused by variations of the charge carrier concentration. Therefore, such difference in Seebeck coefficient could originate from slight deviations from the nominal composition. Interestingly, the magnitude of the Seebeck coefficient can be correlated to the cell parameters (ST_SPS & ST_HP > MA_SPS & MA_HP), that presumably originates from sulfur loss during ST synthesis. Also, as previously shown in other colusite compounds [16,41] it is well accepted that sulfur deficiency can create changes in charge carrier concentration. In the present study, sulfur deficiency reduces the charge carrier concentration, thus explaining the higher Seebeck coefficient of the ST samples as compared to MA synthesized samples.

The temperature dependence of the electrical resistivity for all four samples is given in **Figure 6b**. Over the whole investigated temperature range, the electrical resistivity decreases with increasing temperature, hence displaying a semiconducting behavior. However, it can be presumed from the slight variation of MA_SPS and MA_HP, that the semiconducting behavior is near a transition towards a degenerate semiconductor. In agreement with the Seebeck coefficient, the electrical resistivity at room temperature varies such as: ST_SPS (760 mΩ cm) > ST_HP (640 mΩ cm) > MA_SPS (8.67 mΩ cm) > MA_HP (5.17 mΩ cm). The ST samples exhibit a higher electrical resistivity than the MA samples, consistent with a higher sulfur deficiency, similarly to what was previously reported on colusite [16,23].

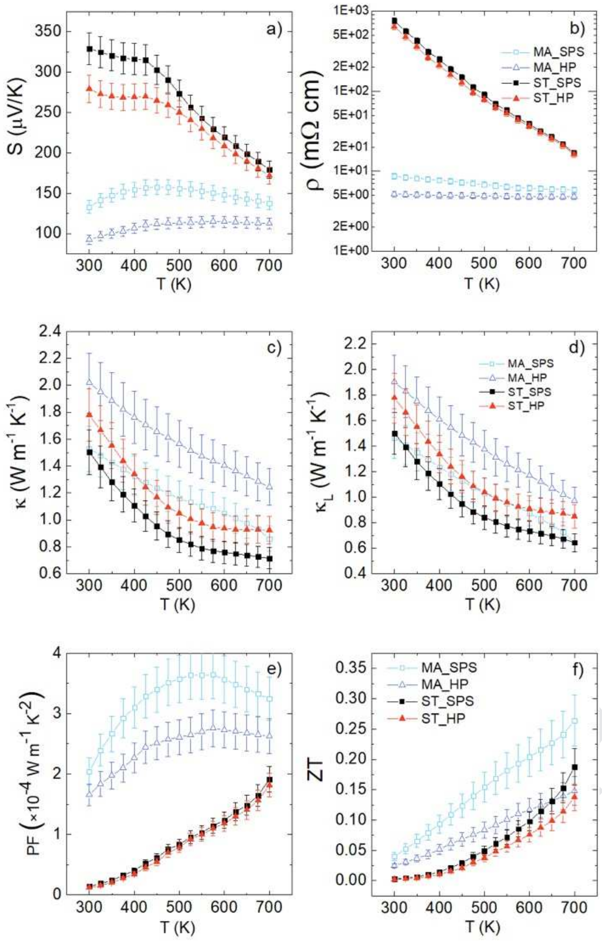

Figure 6. Thermoelectric properties of the four germanite $Cu_{22}Fe_8Ge_4S_{32}$ samples: MA_SPS (squares), MA_HP (triangles), ST_SPS (filled squares) and ST_HP (filled triangles). The thermal evolution of Seebeck coefficient is represented in a), electrical resistivity in b), total thermal conductivity in c), lattice thermal conductivity in d), power factor in e) and figure of merit in f).

The power factor of each sample increases with temperature as seen in **Figure 6e**. MA_SPS sample has the highest power factor with a maximal value of 3.64×10^{-4} W m^{-1} K^{-2} at 550 K followed by MA_HP with a maximum power factor of 2.75×10^{-4} W m^{-1} K^{-2} at 575 K. As evidenced by the relatively low power factor at 700 K of 1.92×10^{-4} W m^{-1} K^{-2} for ST_SPS and 1.81×10^{-4} W m^{-1} K^{-2} for ST_HP, it is probable that the lower carrier concentration in ST samples distances from the optimal value. Unfortunately, it is not possible to confirm this hypothesis as attempts to measure the carrier concentration in the PPMS system under high magnetic field were unsuccessful due to correlation effects. In the light of these results, it is clear that the germanite prepared by ST synthesis are not markedly affected by the sintering process, as opposed to the samples synthesized by MA, which is consistent with the fact the MA samples undergo reactive sintering.

The thermal conductivity (κ) and its lattice contribution (κ_L), in **Figure 6c** and **6d** respectively**,** are decreasing with temperature for all samples over the whole investigated temperature range. No specific trend can be observed regarding the impact of the powder synthesis and/or sintering method, which suggests that the presence of secondary phases and the substantial difference of grain sizes do not have a significant influence on phonon scattering. To investigate further the possible formation of structural defects at the atomic level, especially in sulfur deficient ST samples, TEM studies, including electron diffraction (ED) and high angle annular dark field scanning TEM (HAADF-STEM) were undertaken (**Figure 7**). Several crystallites of MA_HP and ST_HP samples were analyzed. The ST_HP sample should be the one presenting the highest degree of disorder because it is produced by the combination of the synthesis and sintering conditions that promotes the most of sulfur loss. Also, a comparison with MA_HP allows to observe the influence of powder synthesis on the formation of structural disorder. Indeed, as discussed above, it was recently demonstrated that the sulfur sublimation in the closely related $Cu_{26}V_2Sn_6S_{32}$ colusite structure induces atomic-scale defects/disordered states including interstitial sites, anti-sites defects, and site splitting, which function as strong phonon scatterers.[16,41]. However, HR-TEM analyses brought further evidence that samples are well crystallized and ordered, in agreement with XRPD data. Indeed, the main zones of the ED patterns (as exemplified along the $[001]$ and $[\bar{1}11]$ directions) and the corresponding HAADF-STEM images of both MA_HP and ST_HP, show a highly crystallized structure, which can be indexed based on the cubic $P\bar{4}3n$ ($a \sim 10.6$ Å) structure, obtained from XRPD data. The absence of observable structural defects is mainly explained by the lower sintering temperature (873 K in the present study, against 1023 K in disordered colusites) and the difference in cationic site occupancy in germanite-type structure.[16,22,23,41,44,45]

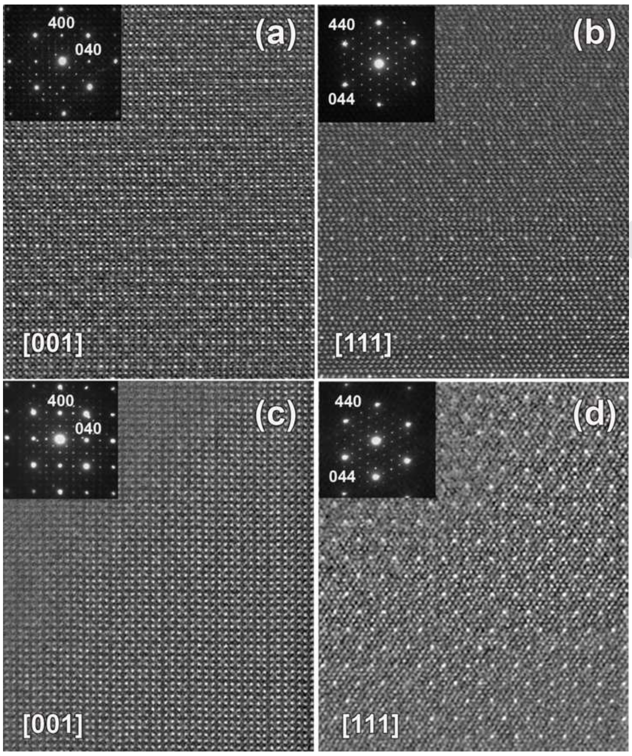

Figure 7. Electron diffraction patterns and micrographs of germanite synthesized by MA_HP along the main crystallographic zone axis a) [001] and b) [111] and germanite synthesized by ST_HP along the main crystallographic zone axis c) [001] and d) [111].

As shown in **Figure 6f**, the dimensionless figure of merit *ZT* for all samples increases with temperature. It appears that the samples synthesized from MA powder have larger ZT values compared with the samples prepared from ST powder. The $ZT_{700\ \mathrm{K}}$ of 0.26 for MA_SPS sample is mainly explained by the lower electrical resistivity due to its higher carrier concentration. Moreover, MA synthesis counts many technical advantages over ST synthesis, such as its low operational temperature and easy scaling up.

Conclusion

This study highlights the importance of the powder synthesis and sintering technique on the structure, microstructure and thermoelectric properties of synthetic germanite $Cu_{22}Fe_8Ge_4S_{32}$. The mechanically alloyed samples present higher *ZT* than the samples prepared by sealed tube synthesis because of their radically lower electrical resistivity due to their higher charge carrier concentration. In opposite, the thermal conductivity is less influenced by the stoichiometry deviations induced by sulfur loss and microstructural changes, or benefits from a competition of effects. Another conclusion is that the ST samples are less affected by the sintering process than the MA samples, which undergo reactive sintering. These results demonstrate once again that mechanical alloying is an effective route to synthesize Cu-based sulfides with high purity and crystallinity after sintering process.

Acknowledgments

The authors gratefully thank J. Lecourt, C. Bilot, C. Couder, S. Gascoin and F. Veillon for technical assistance and the financial support of the French Agence Nationale de la Recherche (Challenge 2, 2015, ANR-15-CE05-0027), FEDER, and Normandy Region.

Disclosure statement

No potential conflict of interest was reported by the authors.

References:

[1] L.E. Bell, Cooling, heating, generating power, and recovering waste heat with thermoelectric systems, Science (80-.). 321 (2008) 1457–1461. https://doi.org/10.1126/science.1158899.

[2] G.S. Nolas, J. Sharp, J. Goldsmid, Thermoelectrics: basic principles and new materials developments, 2013. https://doi.org/10.1038/nphoton.2009.262.

[3] Y. Pei, X. Shi, A. LaLonde, H. Wang, L.L.-D. Chen, G.J. Snyder, Convergence of electronic bands for high performance bulk thermoelectrics, Nature. 473 (2011) 66–69. https://doi.org/10.1038/nature09996.

[4] J.R. Sootsman, D.Y. Chung, M.G. Kanatzidis, New and Old Concepts in Thermoelectric Materials, Angew. Chemie Int. Ed. 48 (2009) 8616–8639. https://doi.org/10.1002/anie.200900598.

[5] K.F. Hsu, Cubic $AgPb_mSbTe_{2+m}$: Bulk Thermoelectric Materials with High Figure of Merit, Science (80-.). 303 (2004) 818–821. https://doi.org/10.1126/science.1092963.

[6] K. Suekuni, K. Tsuruta, T. Ariga, M. Koyano, Thermoelectric Properties of Mineral Tetrahedrites $Cu_{10}Tr_2Sb_4S_{13}$ with Low Thermal Conductivity, Appl. Phys. Express. 5 (2012) 051201. https://doi.org/10.1143/APEX.5.051201.

[7] X. Lu, D.T. Morelli, Y. Xia, F. Zhou, V. Ozolins, H. Chi, X. Zhou, C. Uher, High Performance Thermoelectricity in Earth-Abundant Compounds Based on Natural Mineral Tetrahedrites, Adv. Energy Mater. 3 (2013) 342–348.

https://doi.org/10.1002/aenm.201200650.

[8] W. Lai, Y. Wang, D.T. Morelli, X. Lu, From Bonding Asymmetry to Anharmonic Rattling in $Cu_{12}Sb_4S_{13}$ Tetrahedrites: When Lone-Pair Electrons Are Not So Lonely, Adv. Funct. Mater. 25 (2015) 3648–3657. https://doi.org/10.1002/adfm.201500766.

[9] R. Chetty, A. Bali, M.H.H. Naik, G. Rogl, P. Rogl, M. Jain, S. Suwas, R.C.C. Mallik, Thermoelectric properties of Co substituted synthetic tetrahedrite, Acta Mater. 100 (2015) 266–274. https://doi.org/10.1016/j.actamat.2015.08.040.

[10] P. Lemoine, C. Bourgès, T. Barbier, V. Nassif, S. Cordier, E. Guilmeau, High temperature neutron powder diffraction study of the $Cu_{12}Sb_4S_{13}$ and $Cu_4Sn_7S_{16}$ phases, J. Solid State Chem. 247 (2017) 83–89. https://doi.org/10.1016/j.jssc.2017.01.003.

[11] Y. Kosaka, K. Suekuni, K. Hashikuni, Y. Bouyrie, M. Ohta, T. Takabatake, Effects of Ge and Sn substitution on the metal– semiconductor transition and thermoelectric properties of $Cu_{12}Sb_4S_{13}$ tetrahedrite, Phys. Chem. Chem. Phys. 19 (2017) 8874–8879. https://doi.org/10.1039/c7cp00351j.

[12] D.P. Weller, D.T. Morelli, Rapid synthesis of zinc and nickel co-doped tetrahedrite thermoelectrics by reactive spark plasma sintering and mechanical alloying, J. Alloys Compd. 710 (2017) 794–799. https://doi.org/10.1016/j.jallcom.2017.03.272.

[13] T. Barbier, P. Lemoine, S. Gascoin, O.I. Lebedev, A. Kaltzoglou, P. Vaqueiro, A. V. Powell, R.I. Smith, E. Guilmeau, Structural stability of the synthetic thermoelectric ternary and nickel-substituted tetrahedrite phases, J. Alloys Compd. 634 (2015) 253–262. https://doi.org/10.1016/j.jallcom.2015.02.045.

[14] S. Harish, D. Sivaprahasam, M. Battabyal, R. Gopalan, Phase stability and thermoelectric properties of $Cu_{10.5}Zn_{1.5}Sb_4S_{13}$ tetrahedrite, J. Alloys Compd. 667 (2016) 323–328. https://doi.org/10.1016/j.jallcom.2016.01.094.

[15] T. Barbier, P. Lemoine, S. Martinet, M. Eriksson, M. Gilmas, E. Hug, G. Guélou, P. Vaqueiro, A. V. Powell, E. Guilmeau, Up-scaled synthesis process of sulphur-based thermoelectric materials, RSC Adv. 6 (2016) 10044–10053. https://doi.org/10.1039/C5RA23218J.

[16] C. Bourgès, Y. Bouyrie, A.R. Supka, R. Al Rahal Al Orabi, P. Lemoine, O.I. Lebedev, M. Ohta, K. Suekuni, V. Nassif, V. Hardy, R. Daou, Y. Miyazaki, M. Fornari, E. Guilmeau, High-Performance Thermoelectric Bulk Colusite by Process Controlled Structural Disordering, J. Am. Chem. Soc. 140 (2018) 2186–2195. https://doi.org/10.1021/jacs.7b11224.

[17] Y. Kikuchi, Y. Bouyrie, M. Ohta, K. Suekuni, M. Aihara, T. Takabatake, Vanadium-free colusites $Cu_{26}A_2Sn_6S_{32}$ (A = Nb, Ta) for environmentally friendly thermoelectrics, J. Mater. Chem. A. 4 (2016) 15207–15214. https://doi.org/10.1039/C6TA05945G.

[18] K. Suekuni, H.I. Tanaka, F.S. Kim, K. Umeo, T. Takabatake, Glasslike versus crystalline thermophysical properties of the Cu-S based minerals: Tetrahedrite and colusite, J. Phys. Soc. Japan. 84 (2015) 103601. https://doi.org/10.7566/JPSJ.84.103601.

[19] F.S. Kim, K. Suekuni, H. Nishiate, M. Ohta, H.I. Tanaka, T. Takabatake, Tuning the charge carrier density in the thermoelectric colusite, J. Appl. Phys. 119 (2016) 175105. https://doi.org/10.1063/1.4948475.

[20] K. Suekuni, F.S. Kim, H. Nishiate, M. Ohta, H.I. Tanaka, T. Takabatake, High-performance thermoelectric minerals: Colusites $Cu_{26}V_2M_6S_{32}$ (M = Ge, Sn), Appl. Phys. Lett. 105 (2014) 132107. https://doi.org/10.1063/1.4896998.

[21] C. Bourgès, M. Gilmas, P. Lemoine, N.E. Mordvinova, O.I. Lebedev, E. Hug, V. Nassif, B. Malaman, R. Daou, E. Guilmeau, Structural analysis and thermoelectric properties of mechanically alloyed colusites, J. Mater. Chem. C. 4 (2016) 7455–7463. https://doi.org/10.1039/c6tc02301k.

[22] P. Lemoine, V. Pavan Kumar, G. Guélou, V. Nassif, B. Raveau, E. Guilmeau, Thermal Stability of the Crystal Structure and Electronic Properties of the High Power Factor Thermoelectric Colusite $Cu_{26}Cr_2Ge_6S_{32}$, Chem. Mater. 32 (2020) 830–840. https://doi.org/10.1021/acs.chemmater.9b04378.

[23] C. Candolfi, G. Guélou, C. Bourgés, A.R. Supka, A.R.A.O. Rabih, M. Fornari, B. Malaman, G. LeCaër, P. Lemoine, V. Hardy, R. Zanotti, Jean-Marc Chetty, M. Ohta, E. Koichiro, Suekuni Guilmeau, Disorder-driven glasslike thermal conductivity in colusite $Cu_{26}V_2Sn_6S_{32}$ investigated by Mössbauer spectroscopy and inelastic neutron, Phys. Rev. Mater. Accepted (2020).

~~[24] M.S. Lee, S. Takenouchi, H. Imai, Syntheses of stannoidite and mawsonite and their genesis in ore deposits, Econ. Geol. 70 (1975) 834–843. https://doi.org/10.2113/gsecongeo.70.4.834.~~

[25] V. Pavan Kumar, T. Barbier, V. Caignaert, B. Raveau, R. Daou, B. Malaman, G. Le Caër, P. Lemoine, E. Guilmeau, Copper Hyper-Stoichiometry: The Key for the Optimization of Thermoelectric Properties in Stannoidite $Cu_{8+x}Fe_{3-x}Sn_2S_{12}$, J. Phys. Chem. C. 121 (2017)

16454–16461. https://doi.org/10.1021/acs.jpcc.7b02068.

[26] R.-Z. Zhang, K. Chen, B. Du, M.J. Reece, Screening for Cu–S based thermoelectric materials using crystal structure features, J. Mater. Chem. A. 5 (2017) 5013. https://doi.org/10.1039/c6ta10607b.

[27] P. Qiu, T. Zhang, Y. Qiu, X. Shi, L. Chen, Sulfide bornite thermoelectric material: a natural mineral with ultralow thermal conductivity, Energy Environ. Sci. 7 (2014) 4000–4006. https://doi.org/10.1039/c4ee02428a.

[28] G. Guélou, A. V. Powell, P. Vaqueiro, Ball milling as an effective route for the preparation of doped bornite: Synthesis, stability and thermoelectric properties, J. Mater. Chem. C. 3 (2015) 10624–10629. https://doi.org/10.1039/c5tc01704a.

[29] V. Pavan Kumar, T. Barbier, P. Lemoine, B. Raveau, V. Nassif, E. Guilmeau, The crucial role of selenium for sulphur substitution in the structural transitions and thermoelectric properties of Cu_5FeS_4 bornite, Dalt. Trans. 46 (2017) 2174–2183. https://doi.org/10.1039/C6DT04204J.

[30] S.O.J. Long, A. V. Powell, P. Vaqueiro, S. Hull, High Thermoelectric Performance of Bornite through Control of the Cu(II) Content and Vacancy Concentration, Chem. Mater. 30 (2018) 456–464. https://doi.org/10.1021/acs.chemmater.7b04436.

[31] C. Bourgès, P. Lemoine, O.I. Lebedev, R. Daou, V. Hardy, B. Malaman, E. Guilmeau, Low thermal conductivity in ternary $Cu_4Sn_7S_{16}$ compound, Acta Mater. 97 (2015) 180–190. https://doi.org/10.1016/j.actamat.2015.06.046.

[32] X. Chen, H. Wada, A. Sato, M. Mieno, Synthesis, Electrical Conductivity, and Crystal

Structure of $Cu_4Sn_7S_{16}$ and Structure Refinement of Cu_2SnS_3, J. Solid State Chem. 139 (1998) 144–151. https://doi.org/10.1006/JSSC.1998.7822.

[33] J.-P.F. Jemetio, P. Zhou, H. Kleinke, Crystal structure, electronic structure and thermoelectric properties of $Cu_4Sn_7S_{16}$, J. Alloys Compd. 417 (2006) 55–59. https://doi.org/10.1016/J.JALLCOM.2005.09.030.

[34] V. Pavan Kumar, L. Paradis-Fortin, P. Lemoine, V. Caignaert, B. Raveau, B. Malaman, G. Le Caër, S. Cordier, E. Guilmeau, Designing a Thermoelectric Copper-Rich Sulfide from a Natural Mineral: Synthetic Germanite $Cu_{22}Fe_8Ge_4S_{32}$, Inorg. Chem. 56 (2017) 13376–13381. https://doi.org/10.1021/acs.inorgchem.7b02128.

[35] J. Rodriguez-Carvajal, Recent advances in magnetic structure determination by neutron powder diffraction, Phys. B Condens. Matter. 192 (1993) 55–69. https://www.ill.eu/sites/fullprof/php/reference.html (accessed February 21, 2019).

[36] T. Roisnel, J. Rodríguez-Carvajal, WinPLOTR: A windows tool for powder diffraction pattern analysis, Mater. Sci. Forum. 378 (2001) 118–123. https://doi.org/10.4028/www.scientific.net/MSF.378-381.118.

[37] P. Thompson, D.E. Cox, J.B. Hastings, Rietveld Refinement of Debye-Scherrer Synchrotron X-Ray Data from Al_2O_3., J. Appl. Crystallogr. 20 (1987) 79–83.

[38] H.-S.S. Kim, Z.M. Gibbs, Y. Tang, H. Wang, G.J. Snyder, Characterization of Lorenz number with Seebeck coefficient measurement, APL Mater. 3 (2015) 041506. https://doi.org/10.1063/1.4908244.

[39] E. Alleno, D. Bérardan, C. Byl, C. Candolfi, R. Daou, R. Decourt, E. Guilmeau, S. Hébert,

J. Hejtmanek, B. Lenoir, P. Masschelein, V. Ohorodnichuk, M. Pollet, S. Populoh, D. Ravot, O. Rouleau, M. Soulier, Invited Article: A round robin test of the uncertainty on the measurement of the thermoelectric dimensionless figure of merit of $Co_{0.97}$ $Ni_{0.03}Sb_3$, Rev. Sci. Instrum. 86 (2015) 011301. https://doi.org/10.1063/1.4905250.

[40] R.T. Tettenhorst, C.E.E. Corbato, Crystal Structure of Germanite, $Cu_{26}Ge_4Fe_4S_{32}$, Determined by Powder X-Ray Diffraction., Am. Mineral. 69 (1984) 943–947.

[41] K. Suekuni, Y. Shimizu, E. Nishibori, H. Kasai, H. Saito, D. Yoshimoto, K. Hashikuni, Y. Bouyrie, R. Chetty, M. Ohta, E. Guilmeau, T. Takabatake, K. Watanabe, M. Ohtaki, Atomic-scale phonon scatterers in thermoelectric colusites with a tetrahedral framework structure, J. Mater. Chem. A. 7 (2019) 228–235. https://doi.org/10.1039/c8ta08248k.

~~[42] R. Al Rahal Al Orabi, P. Gougeon, P. Gall, B. Fontaine, M. Colin, C. Candolfi, A. Dauscher, J. Hejtmanek, B. Malaman, B. Lenoir, X □ ray Characterization, Electronic Band Structure, and Thermoelectric Properties of the Cluster Compound $Ag_2Tl_2Mo_9Se_{11}$, Inorg. Chem. 53 (2014) 11699–11709.~~

[43] C. Suryanarayana, Mechanical alloying and milling, Prog. Mater. Sci. 46 (2001) 1–184. https://doi.org/10.1016/S0079-6425(99)00010-9.

[44] V. Pavan Kumar, A.R. Supka, P. Lemoine, O.I. Lebedev, B. Raveau, K. Suekuni, V. Nassif, R. Al Rahal Al Orabi, M. Fornari, E. Guilmeau, High Power Factors of Thermoelectric Colusites $Cu_{26}T_2Ge_6S_{32}$ (T = Cr, Mo, W): Toward Functionalization of the Conductive “Cu–S” Network, Adv. Energy Mater. 9 (2019) 1803249. https://doi.org/10.1002/aenm.201803249.

[45] V. Pavan Kumar, G. Guélou, P. Lemoine, B. Raveau, A. Supka, R. Al Rahal Al Orabi, M. Fornari, K. Suekuni, E. Guilmeau, Copper-rich thermoelectric sulfides: size mismatch effect and chemical disorder in the $[TS_4]Cu_6$ complexes of $Cu_{26}T_2Ge_6S_{32}$ (T = Cr, Mo, W) colusites, Angew. Chemie Int. Ed. 58 (2019) 15455. https://doi.org/10.1002/anie.201908579.

HIGHLIGHTS

Structure, microstructure and thermoelectric properties of germanite-type $Cu_{22}Fe_8Ge_4S_{32}$ compounds

- We highlight the combined effects of powder synthesis and densification on the structure, microstructure and thermoelectric properties of $Cu_{22}Fe_8Ge_4S_{32}$ synthetic germanite compounds
- The changes in the electrical resistivity and Seebeck coefficient with the sample preparation methods evidence the high sensitivity of the material to slight stoichiometric deviations
- We report ZT=0.25 at 700 K in germanite compounds prepared by mechanical alloying and sintered by SPS

Declaration of interests

☒ The authors declare that they have no known competing financial interests or personal relationships that could have appeared to influence the work reported in this paper.

☐The authors declare the following financial interests/personal relationships which may be considered as potential competing interests: